Density effects on nanoparticle transport in the hyporheic zone

Guangqiu Jin [1,2], Qihao Jiang [1,2,4], Hongwu Tang [1,2,#], Ling Li [3], D. A. Barry [4]

[1] State Key Laboratory of Hydrology-Water Resources and Hydraulic Engineering, Hohai University, Nanjing, China. Emails: jingq@hhu.edu.cn, jiangqih@hotmail.com, hwtang@hhu.edu.cn

[2] Centre for Eco-Environmental Modelling, College of Water Conservancy and Hydropower Engineering, Hohai University, Nanjing, China.

[3] School of Civil Engineering, University of Queensland, St. Lucia, Australia. Email: l.li@uq.edu.au

[4] Laboratoire de technologie écologique (ECOL), Institut d'ingénierie de l'environnement (IIE), Faculté de l'environnement naturel, architectural et construit (ENAC), Ecole Polytechnique Fédérale de Lausanne (EPFL), Station 2, 1015 Lausanne, Switzerland. Email: andrew.barry@epfl.ch

[#] Corresponding author, telephone: +86 (25) 8378-6919, fax: +86 (25) 8378-6919

Abstract

A carbon solution composed of nanoparticles (d_{50} = 85.7 nm) was used in experiments designed to explore nanoparticle transport characteristics within the hyporheic zone of a riverbed. Experiments and numerical simulations demonstrated that nanoparticle transport in the hyporheic zone is affected by hydraulic head gradients due to river flow-bedform interactions as well as density gradients associated with the nano-carbon solution. Differences with similar flow/transport situations were examined, and it was found that particulate-enhanced density can change hyporheic transport appreciably. In addition to density, particle settling enhances downward movement of the nano-carbon plume in the riverbed. While nanoparticle transport in the upper hyporheic zone is largely controlled by advection due to flow driven by head gradients at the bed surface, density gradients and particle settling influence the transport process significantly in the lower hyporheic zone. During the transport process, nanoparticles become deposited due to attachment to sand particles and filtration by small pores in the bed. Compared with transport where density variations are minimal, the particulate-induced density gradient induces downward transport of nanoparticles and entrained liquids, leading to deposition/accumulation at the base of the bed.

Keywords: Nanoparticle, hyporheic exchange, density-driven flow, settling, attachment, detachment, bedform

1. Introduction

Engineered nanoparticles in the size range of 1-100 nm are common in the environment [1-4], including in rivers [5-8]. These fine particles have large specific surface areas and associated reactivity, and hence can absorb and carry contaminants [9-11]. Particles can potentially enhance solute transfer to the hyporheic zone where they can be retained, possibly leading to clogging [12, 13] and concomitant changes in the medium's porosity and hydraulic conductivity [14, 15]. The transport and distribution of particles affect not only the mass exchange across the riverbed and hence the river water quality but also the condition of the riverbed habitat [16, 17]. The overall impact of particles on the function and structure of the river ecosystem cannot be overlooked [18-21].

Nanoparticle transport in and across porous riverbeds was investigated previously [9, 22, 23]. *Packman et al.* [24] developed an experimental model for particle exchange between the river and riverbed, which showed that particles with small grain sizes can be trapped by sand. This work was later extended to include a particle exchange model for calculating the effect of particle settling and filtration on net particle exchange [25]. *Boncagni et al.* [9] also examined nanoparticle exchange based on a pumping exchange model, which was validated with experimental data that focused on changes of particle concentration in river water.

In contrast to the abovementioned studies on the river-bedform exchange, in this work we focus attention on nanoparticle transport within the bedform. This aspect was considered by *Karwan et al.* [18], who simulated particle filtration in the hyporheic zone and found that streambed particle filtration depends on stream discharge.

However, particle settling was neglected, as was the effect of variable fluid density due to the presence of nanoparticles.

Like solutes, nanoparticles can change the density of the carrier fluid. Consequently, nanoparticle concentration variations can result in fluid density gradients that affect both fluid flow and mass transport processes [22, 26, 27]. *Jin et al.* [28] showed that such density gradients can accelerate solute transfer from the river water to the riverbed and inhibit the release of solutes from the bed. For nanoparticles, *Kanel et al.* [22] developed a model of nanoparticle transport in porous media that includes density and demonstrated the importance of density during injection of nanoparticles into porous media. *Bonnie et al.* [27] simulated nanoparticle mobility as affected by density gradients in a heterogeneous porous medium and determined that a relatively small contrast in particle density can result in flow instabilities. However, how nanoparticle transport in the hyporheic zone is affected by density gradients in combination with other driving forces remains unclear.

The transport and distribution of nanoparticles in the hyporheic zone, as affected by density gradients, is the focus of the present study. Our main goal is to use careful experiments to elucidate possible effects of nanoparticle-induced density on flow and transport within the hyporheic zone (rather than across the river-bedform interface), and to validate a process-based model using the experimental data. To that end, we conducted a series of laboratory experiments with nanoparticles released at different locations in a (laboratory) riverbed. In addition, a series of column experiments provided calibration data for a simple experiment geometry. The resulting data sets enabled quantification of nanoparticle transport within the bedform as affected by flow, filtration, settling and density gradients. The experimental data were examined

in conjunction with results from numerical simulations, focusing on (i) the different transport pathways for nanoparticles released from different locations of the hyporheic zone, (ii) effects of density gradients due to variations of nanoparticle concentration, and (iii) combined effects of settling, deposition and density gradients on the transport pathways of nanoparticles in the hyporheic zone.

2. Laboratory experiments

2.1 Solutes and nanoparticles

Three types of experiments were performed, viz., (i) tracer transport, (ii) density-affected transport (dissolved solute) and (iii) density-affected transport (nanoparticles). For (i), nonreactive dye FD&C Red 40 (Roha Dyechem Ltd, no effect on fluid density) was used as a visualization aid for solute transport unaffected by density gradients. Below, this is referred to as the passive solute. Transport characteristics of this dye are available [29-31]. For (ii), we chose potassium permanganate (purple in color and high solubility) as the active (i.e., induces density changes) solute in experiments to examine density effects on hyporheic flow and associated solute transport processes. There is negligible adsorption of potassium permanganate by the sand used in the experiments. For nanoparticles (iii), we used carbon ink with particles of $d_{50} = 85.7$ nm (Guizhou Aerospace Nanometer Science and Technology Co Ltd). For convenience, below we refer to the injected materials as solutes.

2.2 Column experiments

A series of solute injection experiments were conducted in vertical sand columns as summarized in Table S1 (where the S means Supplementary Materials, identical sand was used in the flume experiments). The purpose of these experiments was to

determine, under the condition of zero mean flow, the transport behavior of the different solutes, which were used in the subsequent flume experiments. In particular, the importance of fluid density gradients and particle settling in controlling the nanoparticle transport was examined. Uniform sand columns were used. Specifically, homogeneous sand was placed to a depth of 30 cm in cylindrical columns (internal diameter $D = 10$ cm). In each experiment, the column was saturated with ponded surface water maintained at a fixed height (approximately 2.5 cm). After establishing stable experiment conditions, 20 mL of solute was rapidly injected into the sand. The position of the injection point was close to the column wall and approximately 25 cm above the base (Fig.1). The transport of the solute was observed using high-resolution digital camera photos, with images recorded every 15 min for 61 h. Identical experiments were repeated each solute (FD&C Red 40, potassium permanganate and carbon ink), although at different concentrations. Model parameters were calibrated using the experimental results, including the settling velocities and total particle-deposition coefficients for the nanoparticles.
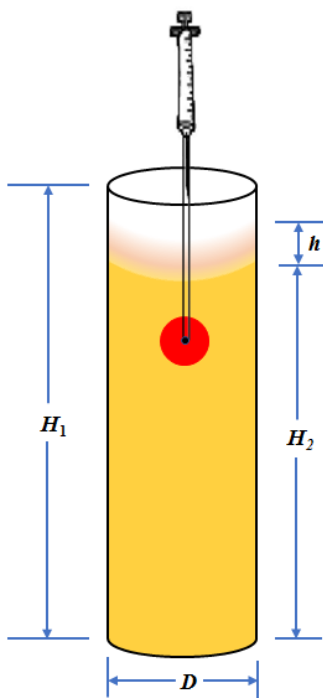

Fig. 1. Schematic diagram of the column experiment set-up, in which solutes were injected into a column that was initially quiescent. $H_1 = 0.35$ m, $H_2 = 0.30$ m, $D = 0.10$ m and $h = 0.025$ m are the column height, sand height, internal diameter of column and overlying water height, respectively.

2.3   Flume experiments

Flume experiments were conducted in a recirculating, tilting flume consisting of an 11.5-m long, 30-cm wide, 50-cm deep rectangular channel (Fig. 2). An artificial sand, with fixed periodic bedforms, was used for the riverbed [26]. In this physical model, water continuously recirculated and flowed over the sediment riverbed. As indicated above, experiments were conducted with non-reactive dye (FD&C Red 40), potassium permanganate and carbon ink under the same flow conditions (Table 1).

Table 1. Conditions of the flume experiments, including flow conditions, bedform geometry and solute concentration (injected into a bedform). The configuration is shown in Figs. 2 and 3.

Case	Streambed depth, d_b (m)	Water depth, H (m)	Stream flow velocity, U (m s^{-1})	Bedform length, L (m)	Bedform height, d (m)	Stoss length, L_c (m)	Initial concentration, C_0 (g L^{-1})
1	0.27	0.13	0.11	0.50	0.10	0.35	0.2
2	0.27	0.13	0.11	0.50	0.10	0.35	2.07
3	0.27	0.13	0.11	0.50	0.10	0.35	10.33

The flume first ran for 0.5 h to establish a quasi-steady flow condition for a given flume slope (slope $S = 0.0006$), thereby achieving the same overlying water depth on all preset bedforms (Fig. 2). Subsequently, 20 mL FD&C Red 40, potassium permanganate or carbon ink was released via (rapid) injection at a preset location (x, y) = (0.27 m, 0.32 m) within the bed (Fig. 3), with subsequent transport captured via digital imagery. We used similar data collection techniques to those previously employed in investigations of the migration of solute plumes affected by density gradients in porous media [22, 27, 32]. Two different concentrations of carbon ink, 2.07 g L^{-1} and 10.33 g L^{-1}, were used to investigate effects of changing density gradients. To avoid interference between experiments (which were conducted

sequentially), different bedforms, selected from the downstream end to the upstream end, were used for injection of different solutes and nanoparticles.
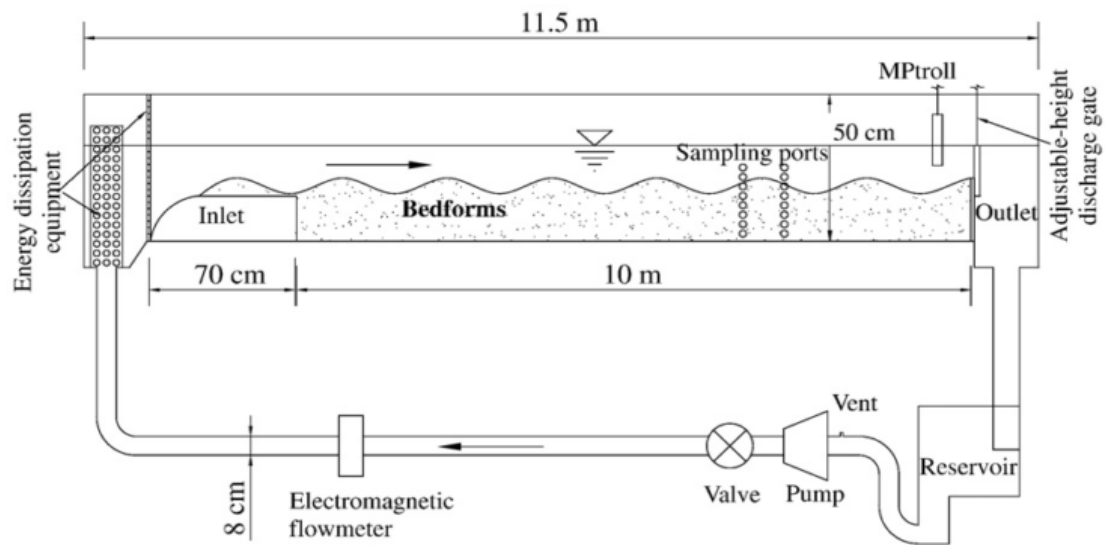

Fig. 2. Schematic diagram of the recirculating flume experiment set-up. Surface water recirculated above fixed bedforms. The water level was measured with an MPtroll unit. Within the bedform, the initial position of tracer injection location was recorded in each case.

2.4 Mathematical models

As in previous studies, one-way sequential coupling was adopted to simulate the river water flow, and pore water flow and solute transport in the riverbed [33-38]. The system was assumed to be homogeneous in the transverse direction, so a 2D numerical model was solved. First, the river water flow was simulated based on the Reynolds-Averaged Navier-Stokes (RANS) equations with the *k-ω* turbulence closure scheme using FLUENT [39]. The pressure distribution predicted by the river water flow model was then used to define the boundary conditions at the sediment-water interface for the pore water flow model. The pore water flow and solute and nanoparticle transport in the bed were then simulated within COMSOL [40] (Fig. 3).
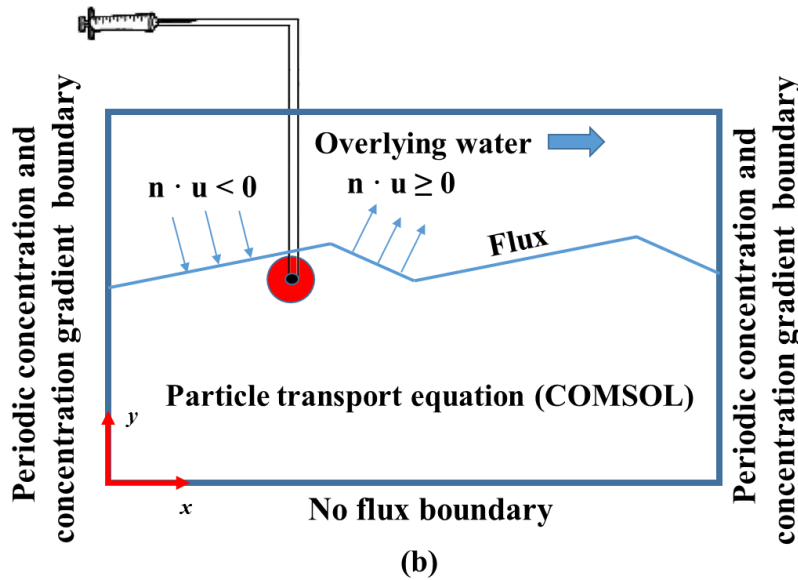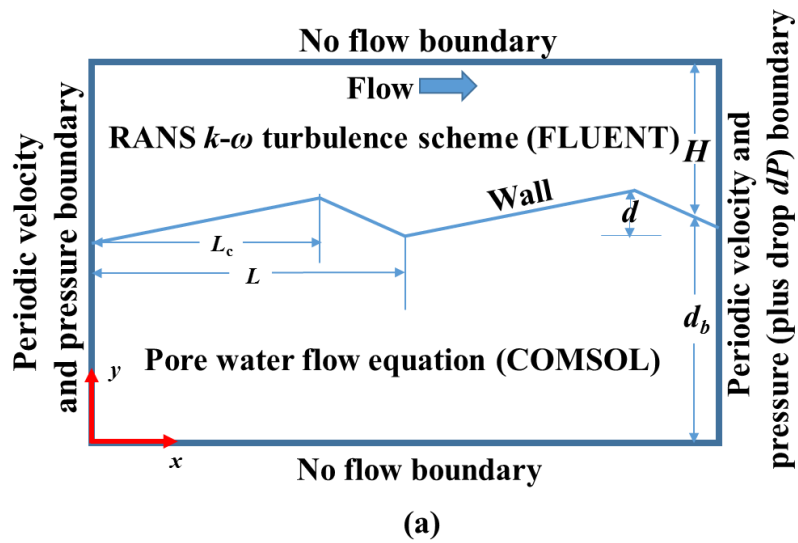
Fig. 3. Model domain and boundaries. (a) For water flow, L, H, d_b, L_c and d are the bedform length, average water depth of overlying water, average depth of streambed, stoss length and bedform height, respectively (Table 1). (b) For nanoparticle transport, the concentration is assumed zero in the overlying water (**n** is the outward normal). Other boundary conditions are described in the text. In all flume experiments, solute was injected within the bedform at the location $(x, y) = (0.27 \text{ m}, 0.32 \text{ m})$, taking the left bottom corner of the bedform as the origin.

The transport model describing nanoparticle movement in the porous bed follows

colloid filtration theory, accounting for density effects [26]. That is, particle transport

and deposition are governed by an advection-dispersion equation with deposition,

attachment of particles to the streambed and settling [25, 41-44]:

$$\frac{\partial C}{\partial t} = \nabla \cdot \left(\mathbf{D} \nabla C - \mathbf{u} C \right) - K_1 C + \frac{K_2}{\theta} S_c$$
$$\frac{1}{\theta} \frac{\partial S_c}{\partial t} = K_1 C - \frac{K_2}{\theta} S_c$$

(1)

where C (kg m^{-3}) is the mobile nanoparticle concentration in the pore water, S_c (kg

m^{-3}) is the concentration of deposited nanoparticles, $\mathbf{D}$ (m^2 s^{-1}) is the hydrodynamic

dispersion tensor, K_1 (s^{-1}) is the total deposition rate coefficient (combines the

attachment and filtration coefficients), K_2 (s^{-1}) is the nanoparticle detachment rate

coefficient, $\mathbf{u}$ (m s^{-1}) is the velocity of nanoparticles, i.e.,

$$\mathbf{u} = -\frac{k}{\mu\theta} (\nabla p + \rho g \mathbf{k}) - v_s \mathbf{k}$$

(2)

where v_s (m s^{-1}) is the nanoparticle settling velocity and $\mathbf{k}$ is the unit vector in the

vertical direction, ρ (kg m^{-3}) is the fluid density, the density-concentration curves for

solutions of potassium permanganate and carbon ink were measured (Fig. 4), k (m^2) is

the riverbed permeability and θ is the porosity. Note that although nanoparticle

trapping can lead to a reduction of the porosity, this effect was minor in the

experiments and thus neglected in the model (i.e., θ and k were assumed to be

constant). In the above model, all flow processes operate in the Darcy regime ($Re <$

1). For solutes, the same transport equation applies with advection and dispersion

terms only.

Boundary conditions for the solute transport were (Fig. 3): (1) on the lateral

boundaries ($x = 0$ and L) of the domain, periodic conditions, $C(0, y ,t) = C(L, y ,t)$

and $\partial C(0, y, t)/\partial y = \partial C(L, y, t)/\partial y$ were imposed; (2) on the bottom of the domain, a no-flux condition was applied, i.e., $\partial C/\partial y = 0$ at $y = 0$; and (3) the concentration in the overlying water remained zero because the quantity of solute/nanoparticle released from the bed was small and so negligibly affected the concentration in the overlying water. Since the transport of solutes and nanoparticles released from one bedform merely extended beyond the two ambient bedforms, only three bedforms were included in the simulations of the experiments.
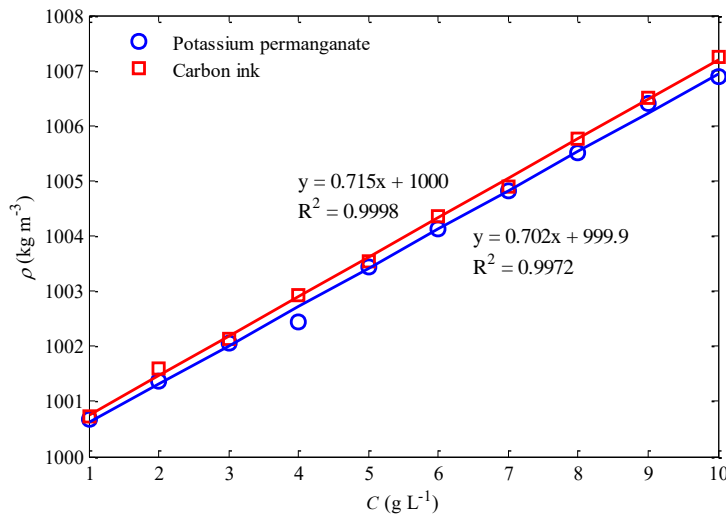

Fig. 4. Density-concentration curves for solutions of potassium permanganate and carbon ink. The regression equations apply to the nearest curve.

3   Results and Discussion

The column experiments (§2.2) were used to calibrate the particle transport model parameters (§2.4); the model was validated with two sets of column experiments (L_2, L_3 of Fig. 9) in Figs. 5-8.

3.1   Model calibration

To construct the nanoparticle transport models in the hyporheic zone, the (constant) parameters (Table 2) for the particle settling velocity (v_s) and the total particle-deposition coefficients (K_1) were calibrated following [45, 46] using images showing the evolution of the column injection experiments. We found that movement of the plume front position (easily extracted from images) was the key attribute for satisfactory model calibration. Comparisons between the experiments and (calibrated parameter values are given in Table S3) model results are presented in Figs. 5-8, concerning which the following observations can be made:

- L_2 in Fig. 5 shows the dispersive transport behavior of the carbon ink in the absence of settling, while $L_3 - L_5$ show spreading along with (enhanced) downward movement of nanoparticles simulated with different settling velocities. Similar behavior is displayed in Fig. 7.

- L_2 in Fig. 6 shows vertical settling of the carbon ink without deposition to the sand. No nanoparticle trail is left following the downward movement. $L_3 - L_6$ show downward movement of nanoparticles with deposition. This movement is inhibited with increasing deposition coefficient. Similar behavior can be seen in Fig. 8.

3.2   Validation of the numerical model with column experiments

Figure 8 shows a series of solute injection experiments conducted in the vertical sand columns for the purpose of validating the transport model and fitted parameter values (§2.4 and 3.1). The fit of the model is considered as satisfactory. Additionally, the following observations of the different cases in Fig. 9 can be made:

- L_1 shows a dispersive transport behavior of the dye plume, as expected for the passive solute (FD&C Red 40).

Table 2. Settling velocities (v_s) and particle-deposition coefficients (K_1) used in the column experiments for the carbon ink (the yellow shading indicates the best-fit value).

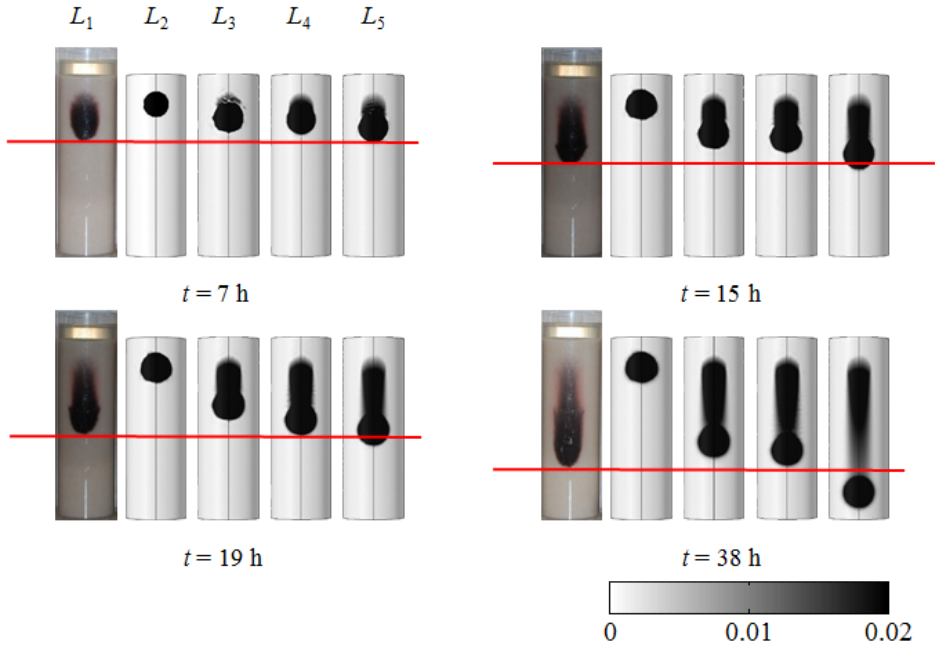| Case (Fig. 5)	C_0 (g L^{-1})	v_s (m s^{-1})	Case (Fig 7)	C_0 (g L^{-1})	v_s (m s^{-1})
A1	0.41	0	A5	2.07	0
A2	0.41	9×10^{-7}	A6	2.07	9×10^{-7}
A3	0.41	1×10^{-6}	A7	2.07	1×10^{-6}
A4	0.41	2×10^{-6}	A8	2.07	2×10^{-6}
Case (Fig. 6)	C_0 (g L^{-1})	K_1 (s^{-1})	Case (Fig. 8)	C_0 (g L^{-1})	K_1 (s^{-1})
B1	0.41	0	B6	2.07	0
B2	0.41	3×10^{-6}	B7	2.07	3×10^{-6}
B3	0.41	5×10^{-6}	B8	2.07	5×10^{-6}
B4	0.41	9×10^{-6}	B9	2.07	9×10^{-6}
B5	0.41	2×10^{-5}	B10	2.07	2×10^{-5}

Fig. 5. Comparison of experimental (L_1) and numerical modeling ($L_2 - L_5$) results for nanoparticles in vertical columns (Table 2). From left to right: 0.41 g L^{-1} carbon ink and 0.20 g L^{-1} FD&C Red 40 for experiment (L_1), 0.41 g L^{-1} carbon ink for simulation with $v_s = 0$ (L_2), 9×10^{-7} m s^{-1} (L_3), 1×10^{-6} m s^{-1} (L_4) and 2×10^{-6} m s^{-1} (L_5). The line indicates the key metric for the calibration, i.e., agreement between the modeled and measured front position.
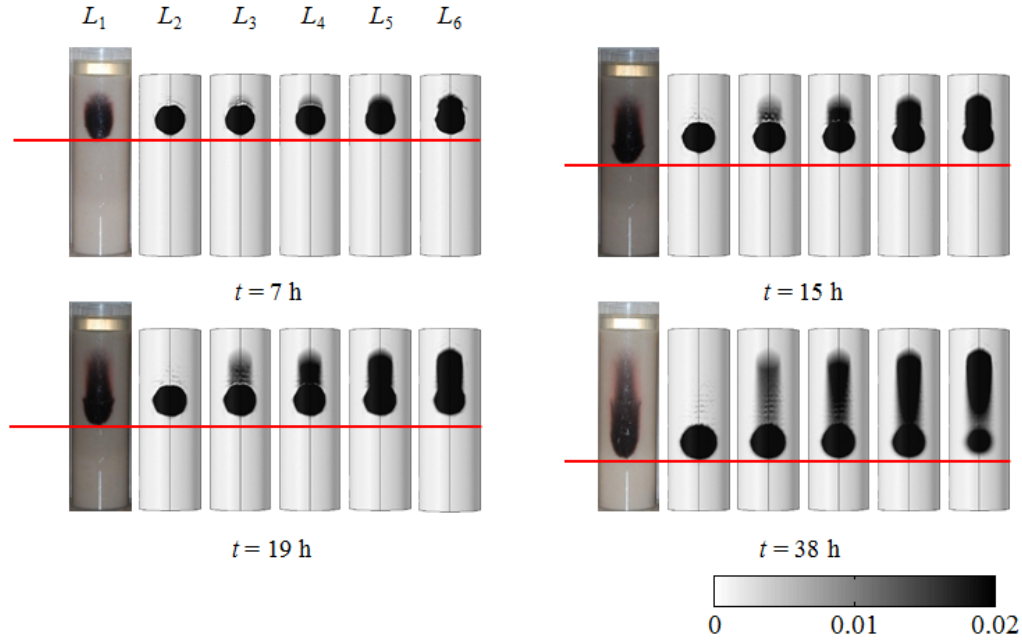
Fig. 6. Comparison of experimental (L_1) and numerical modeling ($L_2 - L_6$) results for nanoparticles in vertical columns (Table 2). From left to right: 0.41 g L^{-1} carbon ink and 0.20 g L^{-1} FD&C Red 40 (L_1), 0.41 g L^{-1} carbon ink for simulation with different deposition coefficients, viz., 0 (L_2), 3×10^{-6} s^{-1} (L_3), 5×10^{-6} s^{-1} (L_4), 9×10^{-6} s^{-1} (L_5), 2×10^{-5} s^{-1} (L_6). The line indicates the key metric for the calibration, i.e., agreement between the modeled and measured front position.
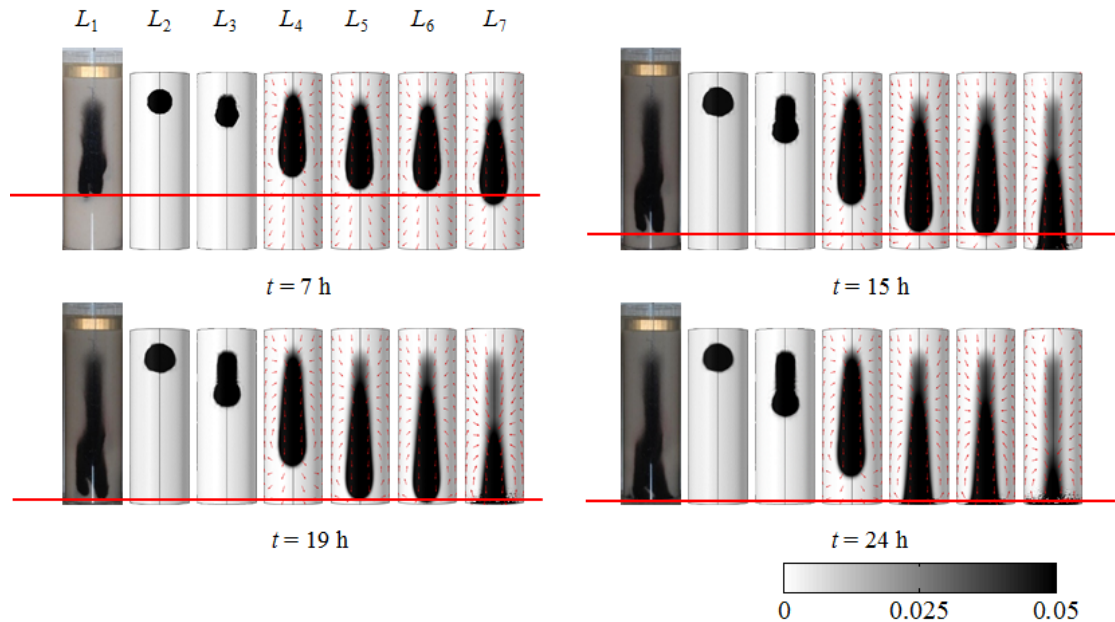

Fig. 7. Comparison of experimental (L_1) and numerical modeling ($L_2 - L_7$) results for nanoparticles in vertical columns (Table 2). Arrows show the computed flow directions. From left to right: 2.07 g L^{-1} carbon ink and 0.20 g L^{-1} FD&C Red 40 (L_1), simulation for: 2.07 g L^{-1} carbon ink without density variations and $v_s = 0$ (L_2), 2.07 g L^{-1} carbon ink without density variation and $v_s = 9 \times 10^{-7}$ m s^{-1} (L_3), density variations and $v_s = 0$ (L_4), 9×10^{-7} m s^{-1} (L_5), 1×10^{-6} m s^{-1} (L_6), 2×10^{-6} m s^{-1} (L_7). The line indicates the key metric for the calibration, i.e., agreement between the modeled and measured front position.
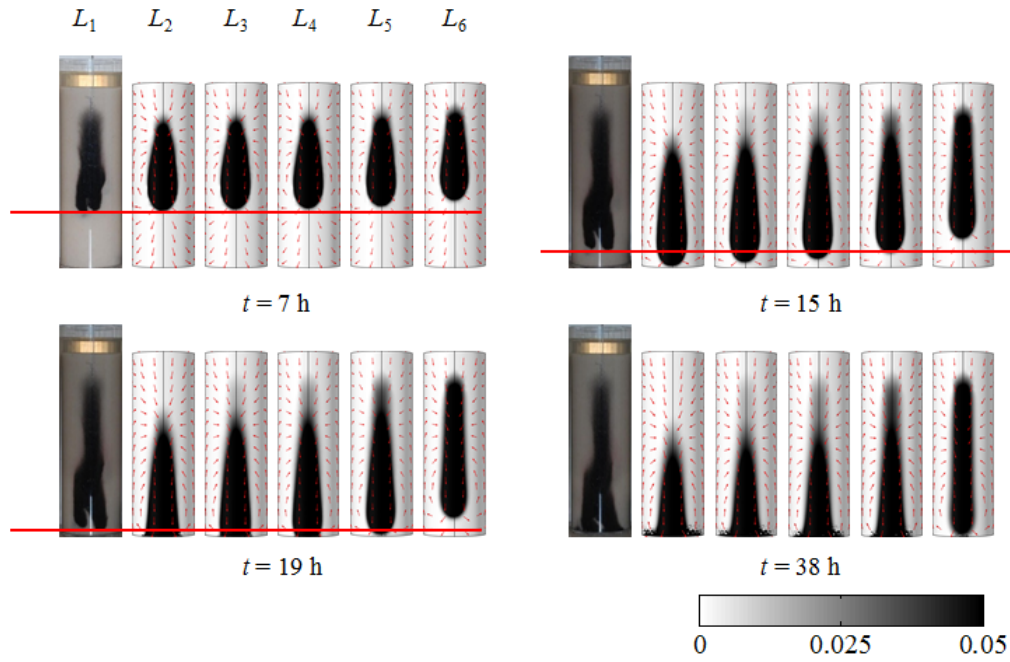
Fig. 8. Comparison of experimental (L_1) and numerical modeling ($L_2 - L_6$) results for nanoparticles in vertical columns (Table 2). Arrows show the computed flow directions. From left to right: 2.07 g L^{-1} carbon ink and 0.20 g L^{-1} FD&C Red 40 (L_1), 2.07 g L^{-1} carbon ink for simulation with different deposition coefficients, viz., 0 (L_2), 3×10^{-6} s^{-1} (L_3), 5×10^{-6} s^{-1} (L_4), 9×10^{-6} s^{-1} (L_5), 2×10^{-5} s^{-1} (L_6). The line indicates the key metric for the calibration, i.e., agreement between the modeled and measured front position.

- $L_2 - L_5$ also show spreading along with downward movement of nanoparticles. As demonstrated by the numerical model, the downward movement of the plume was due to the combined influence of density gradient-driven flow and nanoparticle settling (Figs. 5 and 6). The density gradient increased with increasing concentration of the injected nanoparticle-fluid mixture, and accordingly so did transport due to this gradient. The trace left behind indicates the effect of particle attachment/filtration.

- L_6 shows not only spreading (dispersion) of the potassium permanganate solute but also a downward movement of the plume with time. The downward movement is due to flow driven by the fluid density gradients.
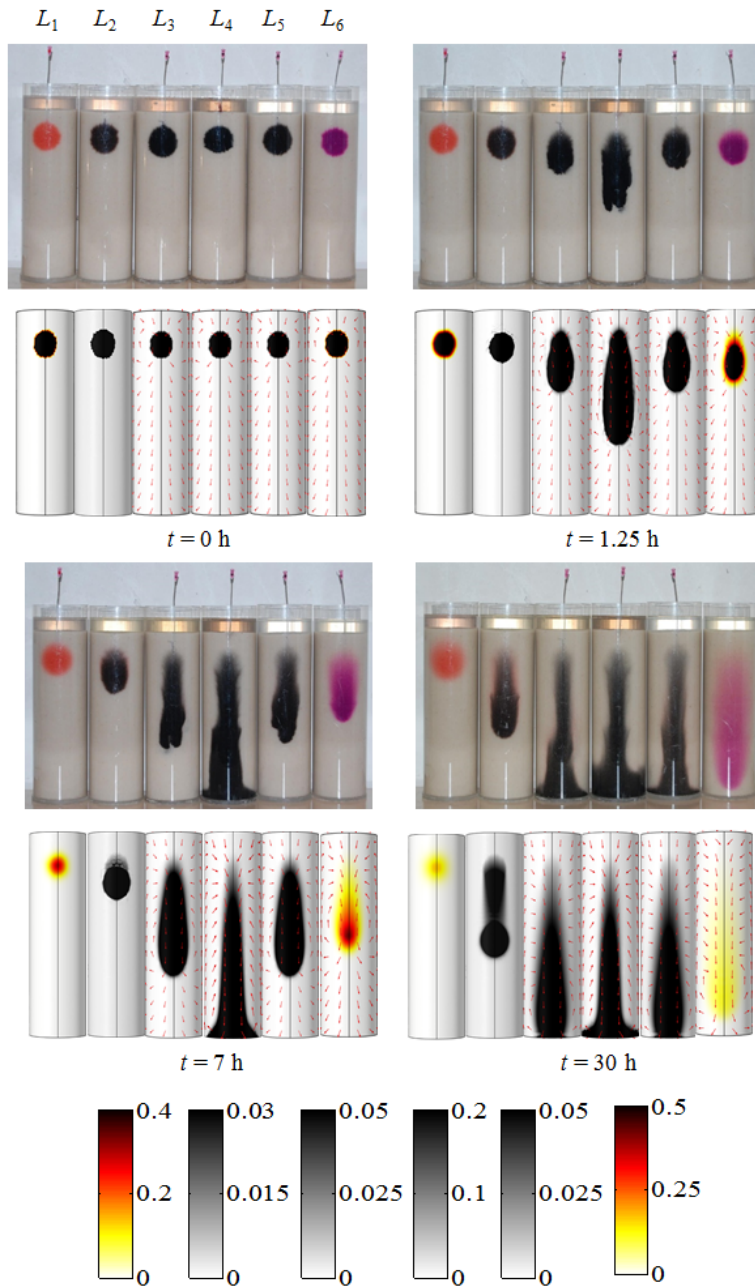
Fig. 9. Comparison of experimental and numerical modeling results for solutes and nanoparticles in vertical columns. Arrows show the computed flow directions. From left to right: 0.41 g L^{-1} FD&C Red 40 (L_1), 0.41 g L^{-1} carbon ink (nano-carbon solute) and 0.20 g L^{-1} FD&C Red 40 (L_2), 2.07 g L^{-1} carbon ink and 0.20 g L^{-1} FD&C Red 40 (L_3), 10.33 g L^{-1} carbon ink and 0.20 g L^{-1} FD&C Red 40 (L_4), 2.07 g L^{-1} carbon ink with 0.20 g L^{-1} FD&C Red 40 (L_5, repeating L_3), 2.07 g L^{-1} potassium permanganate (L_6). Experimental and numerical modeling results are shown on the top and bottom rows, respectively.
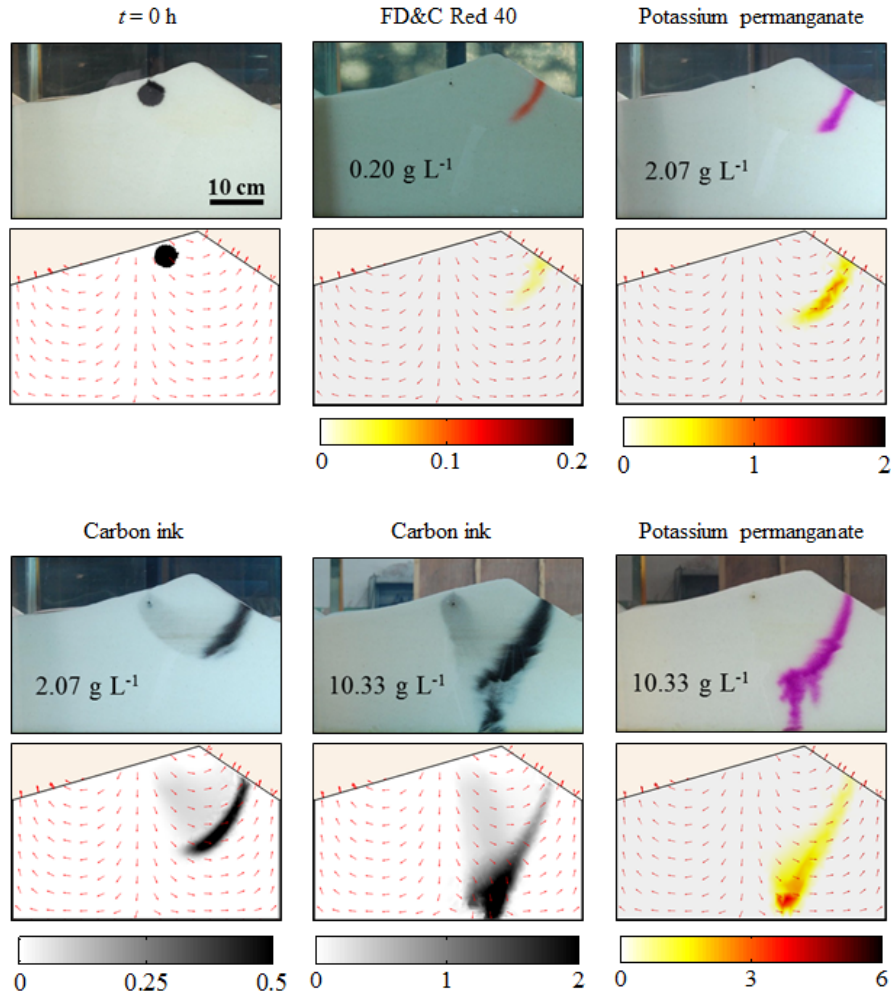
Fig. 10. Comparison of solutes and nanoparticle distributions in the bed from experiments and numerical modeling ($t = 2$ h). Arrows show the computed flow directions. The injection point was located below the stoss slope of the bedform as indicated by the black point $(x, y) = (0.27$ m, 0.32 m). In the overlying water, the flow direction was from left to right. Experimental and modeling results are shown on the 1st and 3rd rows, and 2nd and 4th rows, respectively. The top two rows in the first column show the initial condition. The other figures show results at $t = 2$ h.

3.3   Transport of solutes and nanoparticles in the hyporheic zone

The experiments permit identification of the roles of different transport mechanisms, due to use of passive and active solutes and nanoparticles. The results from the flume experiments and numerical simulations show these differences in a consistent manner (Fig. 10).

The passive solute (FD&C Red 40) largely followed the pore water flow path in the hyporheic zone (Fig. S1a), moving from the injection point under the stoss slope of the platform to the exit at the lee slope. In the experiment with potassium permanganate, the increased density relative to the passive solute changed the flow field, which in turn modified the solute transport path. In particular, for high solute concentrations, the induced density gradient produced a downward flow that moved the solute to the bottom of the bed (Fig. S1c). As a result, only a small amount (24% based on the simulation results) of solute exited the bed. As the solute plume moved downward, the flow field was modified by density gradients particularly near the solute front. An additional feature of the simulations is that the background flow field (e.g., as shown for the FD&C Red 40 tracer) is predominantly horizontal near the top of the bedform, becoming more vertically oriented with depth. For injected solutes with increasing density, the initial strong vertical gradient due to negative buoyancy moves the solute into an area with a background flow that is more oriented downwards than laterally. The two effects (negative buoyancy and greater background vertical flow component) combine to promote downward movement of the solute, increasing the likelihood of subsequent trapping at the base of the bedform. This behavior is observed also for the nanoparticle transport.

Nanoparticle transport is similar to that of the potassium permanganate solute. The evolution of the nanoparticle plume shows clearly the density effect, which increases with increasing particle concentration (Figs. S1d and e). The simulations further demonstrate the influence of particle settling, which also played a role in the downward movement of nanoparticles (Fig. S2). In contrast to the solute transport, the nanoparticle movement left behind traces of particles deposited in the porous medium.

The numerical simulation also revealed significant effects of nanoparticles on the flow field in the form of density gradients.
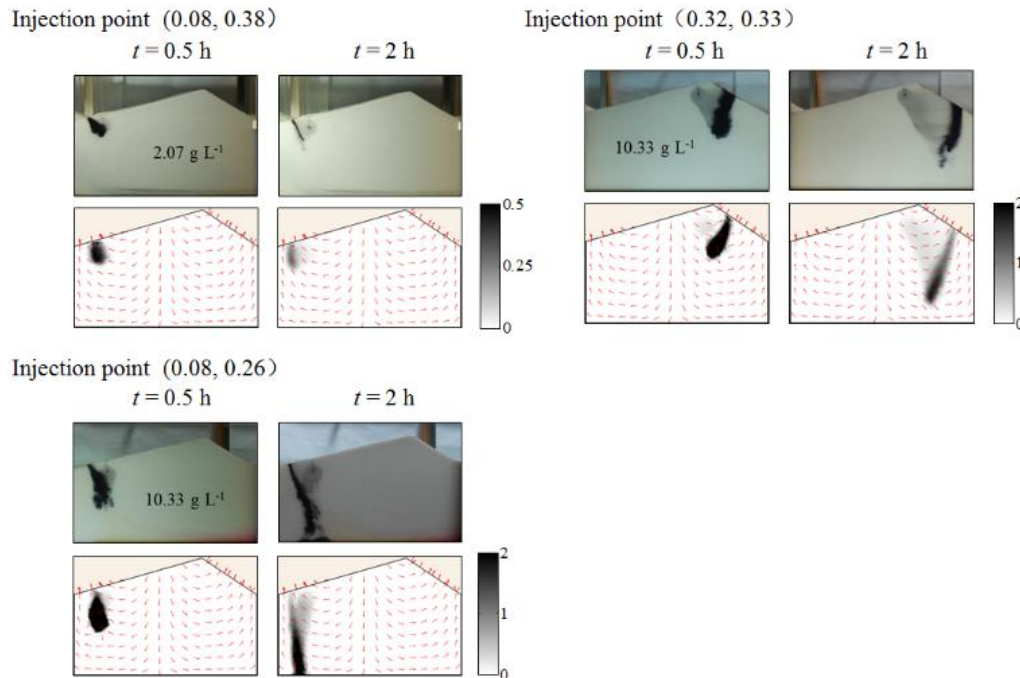

Fig. 11. Comparison of experimental and modeled nanoparticle distributions in the bed at different times for cases three different carbon solution injection locations (location units are m). Arrows show the computed flow directions.

Experiments were also conducted with nanoparticles released from different locations in the streambed (Fig. 11). Again, the numerical model reproduced the observations well. Density gradients associated with the nanoparticle concentrations affect significantly the transport of nanoparticles, producing an overall downward particle movement. This may lead to permanent retention of nanoparticles in the riverbed in addition to particles deposited in the porous medium due to attachment and filtration. Both the experiments and simulations showed that in the cases with the potassium permanganate and nanoparticles, flow instability could occur when the concentration-
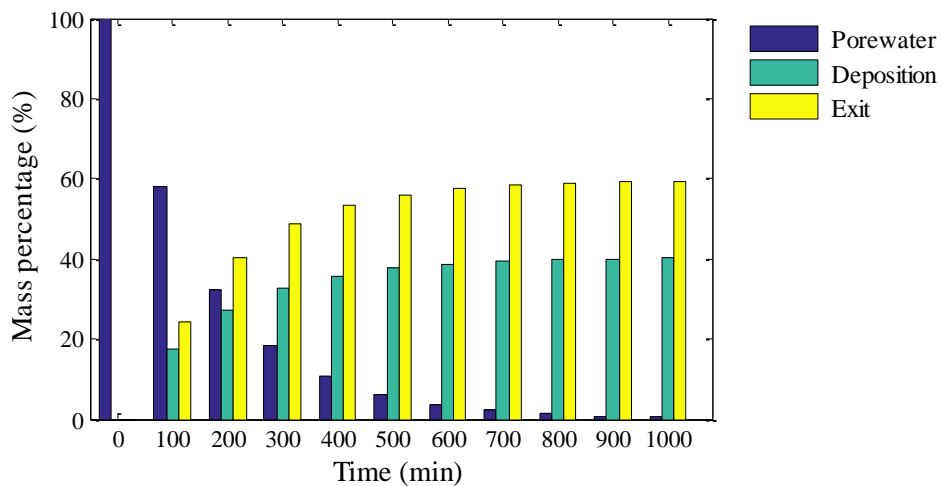
(a)
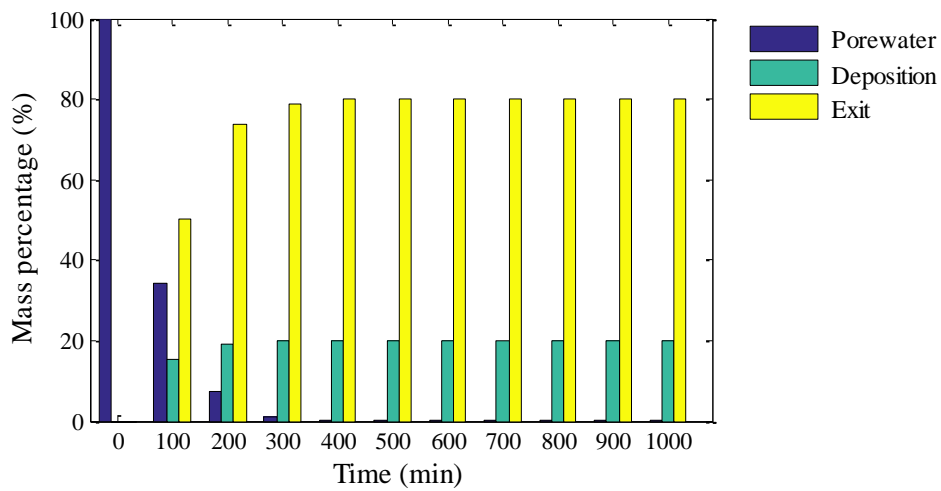
(b)

Fig. 12. Mass budget of nanoparticles released at different initial concentrations, (a) 2 g L^{-1}, (b) 10g L^{-1}.

induced density gradients became sufficiently large. Flow instability led to the formation of fingers in the plumes, which enhanced mixing of solute or particle plumes with ambient water. The mass budget of nanoparticles (deposition, in pore water, or exited to the stream, Fig. 12) was calculated using simulation results for the case of low (2 g L^{-1}) and high concentration (10 g L^{-1}). Shortly after the particles were released, the mass percentage of deposition for the high concentration case was higher

than for low concentration due to the longer travel path and residence time within bedform, and a corresponding long-term decrease of nanoparticles in the pore water.

3.4 Mass percentage of deposited and released particles, residence time and spatial moments

Based on the numerical simulation results, we examined how the nanoparticle trapping depends on the initial particle concentration at the release point (Fig. 13a1, cf. 13a2). An increase in C_0 (case of $C_0 = 10$ g L^{-1}, cf. case of $C_0 = 2$ g L^{-1}) led to larger upward density gradients at the front of the plume, which drove the pore water and nanoparticles to move downward. This resulted in a lengthened particle travel path (Fig. S6). Particle trapping occurred along the travel path and the amount of deposited particles (m_s^*, percentage of the initial amount) increased with time (Fig. 13b). The same increasing trend was observed initially in both cases since the particle movement at this stage was controlled by the surface head gradient-driven flow (consistent with the results shown in Fig. 12). Later ($t > 40$ min), the particles moved further down along an extended path in the case of $C_0 = 10$ g L^{-1}, resulting in more particles deposited in the bed (Fig. 13b). From model results (Fig. 13b), we can assess that 20% and 40% of the nanoparticles can deposit permanently (on the time scale of the experiment) to sand for initially low ($C_0 = 2$ g L^{-1}) and high concentrations ($C_0 = 10$ g L^{-1}), respectively. Previous observations of carbon nanoparticle deposition in porous media through a series of column experiments found similar proportions of deposited particles [23, 47, 48]. There was a weak net flow across the bedform and so particles that reached the bottom of the bed could still move (albeit slowly) to exit the bedform from the side boundary, i.e., no particles, except those that were deposited,

were retained within the bedform as simulated (Fig. 13b). In reality, nanoparticles driven by the density gradients to move downward potentially remain in the bed.

In the model, two particle-specific processes, settling and trapping (Table S4) predict different nanoparticle transport behaviors. Settling can enhance transport to the deeper portions of the bed (Fig. 13a2, a3), but does not noticeably cause additional trapping (Fig. 13b). Trapping removes particles from the pore water, resulting in a lower percentage of particles escaping the bed. This is seen in Fig. 10, where a carbon ink plume trail is left behind (in contrast to the case of potassium permanganate). Taken over the whole hyporheic zone, and before solute exits this zone (i.e., on a short time scale), from Eq. (1) it is clear that the mass of solute being transported in the hyporheic zone reduces exponentially (proportional to K_1 if $K_2 = 0$), as suggested by the results in Fig. 13. The solute leaving the hyporheic zone (Fig. 10) also reduces the mass within this zone, approximately exponentially and dependent on the flux across the domain boundary (Fig. 3b). Thus, the total mass of solute undergoing liquid phase transport in the hyporheic zone is approximately described by a mixture of exponential terms, which is, again, evident from Fig. 13c. Correspondingly, the total mass of trapped particles also shows a mixed exponential behavior (Fig. 13b).

The experiments did not run sufficiently long to determine if the nanoparticles would eventually be flushed from the hyporheic zone (i.e., the deposited particle plume trails remain in the sand at the end of the experiment). This is consistent with the plateauing of the modeled deposition mass curve in Fig. 13b, which due to taking $K_2 = 0$ in Eq. (1), i.e., particle detachment was not included in the simulations of the experimental results. Taking both K_1 and $K_2 \neq 0$ straightforwardly shows the effect of nanoparticle detachment. To this end, we take different ratios between attachment and detachment to show how the maximum deposition mass percentage within the hyporheic changes

due to the corresponding release of deposited nanoparticles from the bed (Fig. 14).

Overall, the combined effect of attachment and detachment changes migration rates of

mobile nanoparticles in the pore water to different degrees. For example, for $C_0 = 10$ g

L^{-1} and $K_2 = K_1 = 9 \times 10^{-6}$ s^{-1}, it took approximately 750 min for the injected

nanoparticles to be removed from the system. For this case, there was also a 9.8%

increase in the mean path length and a 9.0% increase in the residence time within the

bedform (Table S4a).

A further series of simulations was conducted to explore how density-gradient,

nanoparticle deposition and settling combine to influence the transport and

distribution in the bed. The centroid was determined based on the simulation results as

follows (e.g., [49]),

$$\overline{X} = \frac{\iint xC(x,y,t)dxdy}{\iint C(x,y,t)dxdy} \tag{3}$$

$$\overline{Y} = \frac{\iint yC(x,y,t)dxdy}{\iint C(x,y,t)dxdy} \tag{4}$$

The results (Fig. 15a-c) demonstrate the important coupling effects of these

mechanisms on the behavior of nanoparticles in the riverbed. Density gradients lead to

downward movement of nanoparticles, which is enhanced by particle settling (Fig.

15a, cf. Fig. 15b). As shown in Table S4a, the mean nanoparticle travel distance and

residence time was increased by 9.7% and 28.3%, respectively ($v_s = 0$, cf. $v_s = 1 \times 10^{-6}$

m s^{-1}). These increases also result in increased particle deposition (Table S2a, b),

which in turn produces a negative feedback as the travel distance increases by

reducing density gradients of water-borne nanoparticles. Not surprisingly,

nanoparticle travel paths differ from the pore water streamlines (Fig. 15a, cf. Fig.

15c), as shown in Table S4a where there was a 7.6% and 21.7% decline in mean travel distance and residence time, respectively ($K_1 = 0$, cf. $K_1 = 2 \times 10^{-5}$ s^{-1}). Here, for some cases (e.g., $C_0 = 10$ g L^{-1}, $K_1 = 0$), the residence time becomes very large since the mean travel path reaches the bottom of the bedform and remains there (on the time scale of the simulation).
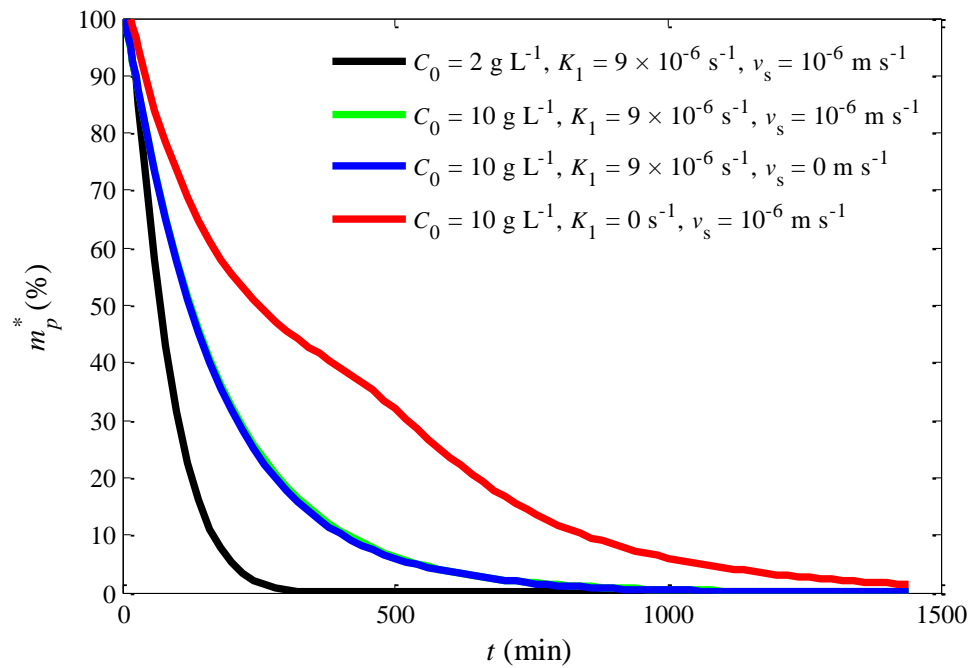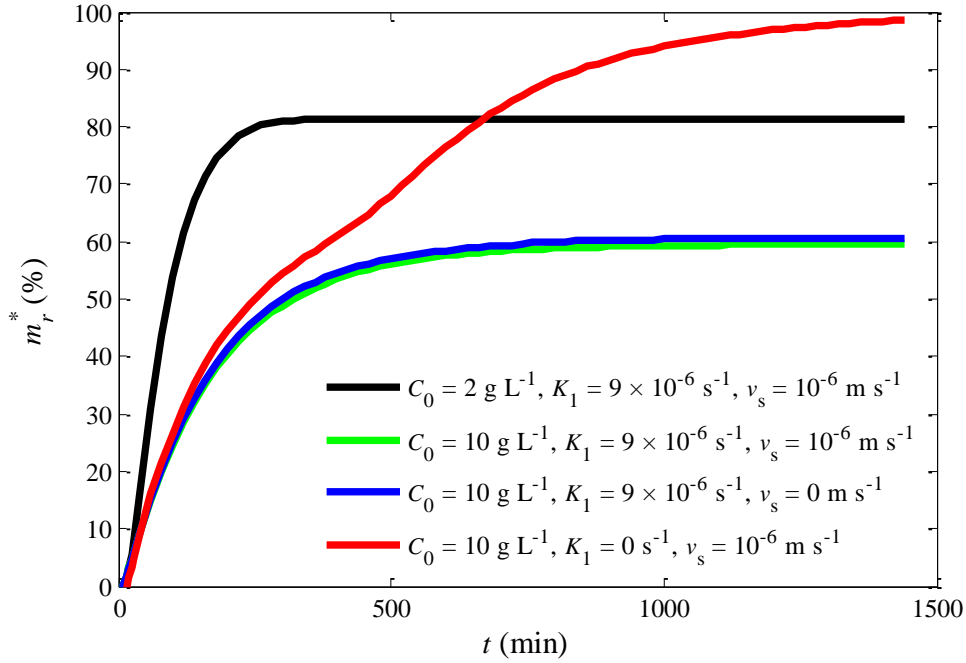
(a)
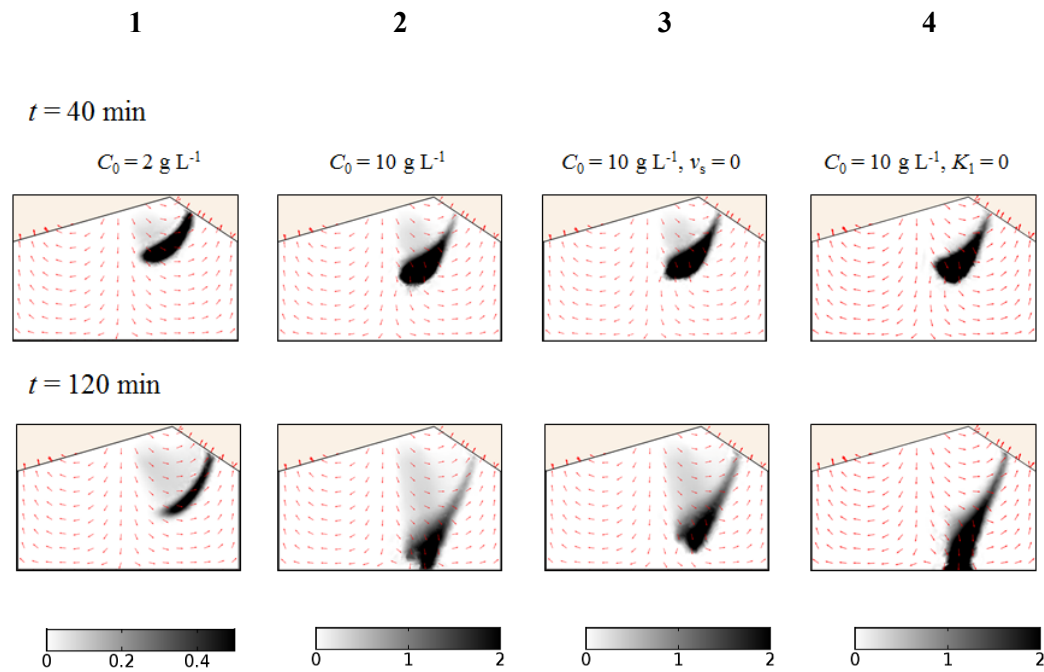
(b)
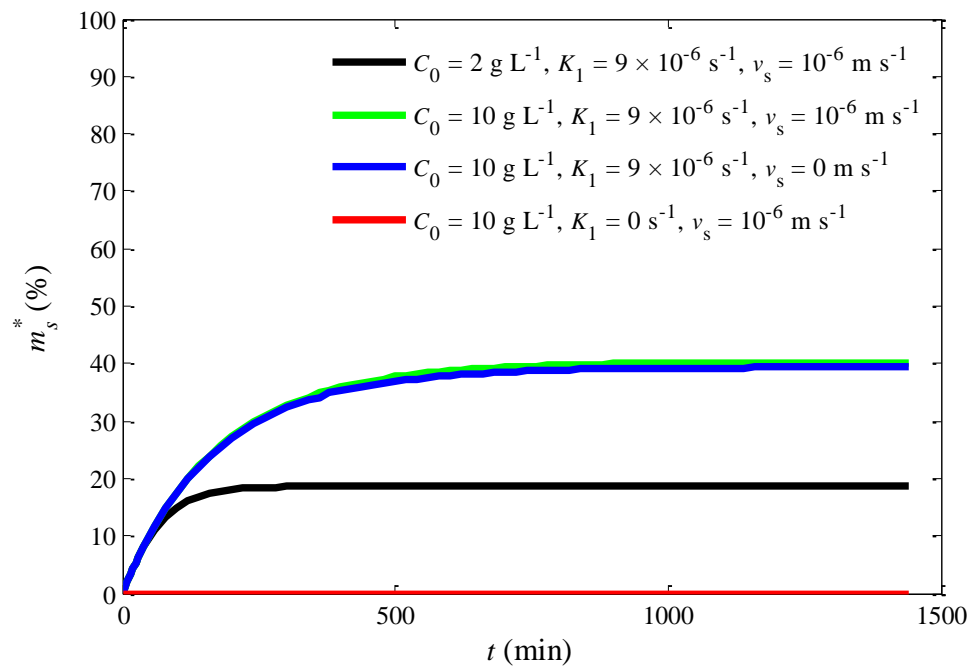
(c)

(d)

Fig. 13. (a) Traces of the deposited particles at different times for different cases. (b) Mass percentage of deposited particles (m_s^*) varying with time for different cases. (c) Mass percentages of particles that remained in pore water of the bed (m_p^*). (d) Note that $1 - m_s^* - m_p^*$ gives the mass percentage of particles that exit the bed.
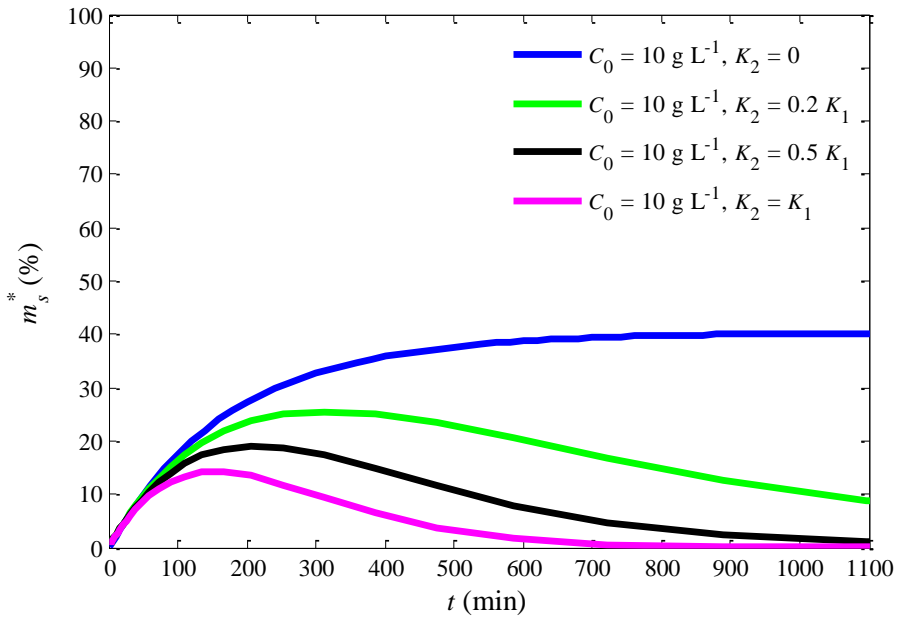

Fig. 14. Mass percentage of deposited particles (m_s^*) varying with time for different ratios between attachment and detachment and taking $K_1 = 9 \times 10^{-6}$ s^{-1}.

In any experiment, small variations in packing can change hydraulic conductivity and porosity values, which can affect initiation and movement of an unstable plume [50]. We explored the impact of these two parameters on the transport behavior. As expected, the results showed that these two parameters can increase or decrease the nanoparticle rate of movement, along with that of pore water within the bedform. On the other hand, these parameters did not substantively modify the transport path as was the case for parameters affecting nanoparticle settling and deposition (Fig. S4, cf. Fig. S3). There was a concomitant change in mean nanoparticle travel distance and residence (Table S4).
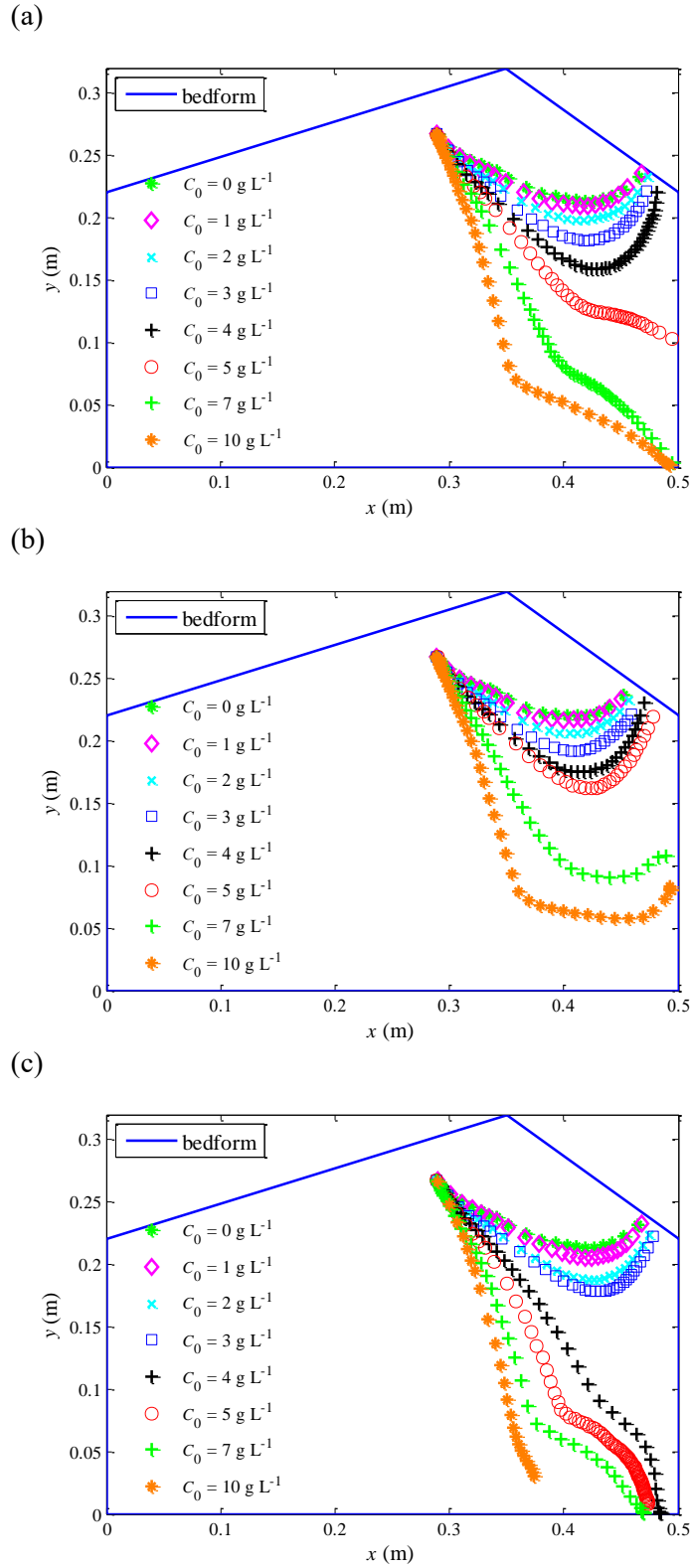
(a)

(b)

(c)

Fig. 15. Centroids of nanoparticles moving in the bed simulated under different initial concentrations with (a) $K_1 = 9 \times 10^{-6}$ s^{-1}, $v_s = 10^{-6}$ m s^{-1}; (b) $K_1 = 9 \times 10^{-6}$ s^{-1}, $v_s = 0$ m s^{-1}; (c) $K_1 = 0$ s^{-1}, $v_s = 10^{-6}$ m s^{-1}.

4   Conclusions

We conducted experiments and numerical simulations to examine nanoparticle transport in the hyporheic zone of a riverbed. The combined experimental/numerical approach shows that:

- The downward particle movement is enhanced by the particle settling, whether or not instability is evident. Nanoparticle transport is influenced by the hyporheic flow induced not only by pressure variations on the riverbed surface but also density gradients due to variable nanoparticle concentrations, which tend to drive the negatively buoyant particles downward.

- Deposition is due to attachment to sand particles and filtration by small pores. A considerable amount of nanoparticles is deposited inside the bed; particle deposition also produces a negative feedback by reducing density gradients.

- A relatively simple model is capable of describing the movement and deposition of nanoparticles in the hyporheic zone.

- Under the influence of density gradients, nanoparticles move downward and can accumulate at the bottom of the bed, with little macroscopic movement thereafter.

- For a negatively buoyant nanoparticle plume entering the bedform from the overlying water, the entry point to the bedform is important since the direction of motion of the background flow is varies along the bedform/river interface.

- Furthermore, in our experiments wherein solute is injected into the bedform, the initial density gradient (due to the solute concentration and background flow field) can enhance the initial movement of the injected material such that it moves from a location where the background flow is mainly lateral and exits the medium, to a zone where the flow is mainly vertical and so the solute moves to the base of the bedform.

The present study focused on the transport behavior of nanoparticles from a point source in the bed. Investigations into dense nanoparticle plumes traversing the river/bedform interface are needed to quantify the rate at which particles are transported into and out of the riverbed, which would complement the present study that elucidated the different possible transport pathways of nanoparticles in variably density plumes within the hyporheic zone.

Acknowledgments

References

1   Sajid M, Ilyas M, Basheer C, Tariq M, Daud M, Baig N, Shehzad F (2015), Impact of nanoparticles on human and environment: Review of toxicity factors, exposures, control strategies, and future prospects. Environmental Science and Pollution Research. 22(6): 4122-4143. http://dx.doi.org/10.1007/s11356-014-3994-1.

2   Maurerjones M A, Gunsolus I L, Murphy C J, Haynes C L (2013), Toxicity of engineered nanoparticles in the environment. Analytical Chemistry. 85(6): 3036-3049. http://dx.doi.org/10.1021/ac303636s.

3   Li L, Fan M, Brown R C, Leeuwen J V, Wang J, Wang W, Song Y, Zhang P (2006), Synthesis, properties, and environmental applications of nanoscale iron-based materials: A review. Critical Reviews in Environmental Science and Technology. 27(5): 405-431. http://dx.doi.org/10.1080/02603590500496721.

4   Goswami L, Kim K-H, Deep A, Das P, Bhattacharya S S, Kumar S, Adelodun A A (2017), Engineered nano particles: Nature, behavior, and effect on the

environment. Journal of Environmental Management. 196:297-315. http://dx.doi.org/https://doi.org/10.1016/j.jenvman.2017.01.011.

5   Zhou D, Abdel-Fattah A I, Keller A A (2012), Clay particles destabilize engineered nanoparticles in aqueous environments. Environmental Science and Technology. 46(14): 7520-7526. http://dx.doi.org/10.1021/es3004427.

6   Adam V, Loyaux-Lawniczak S, Labille J, Galindo C, del Nero M, Gangloff S, Weber T, Quaranta G (2016), Aggregation behaviour of TiO$_2$ nanoparticles in natural river water. Journal of Nanoparticle Research. 18(1): 11-21. http://dx.doi.org/10.1007/s11051-015-3319-4.

7   Petosa A R, Jaisi D P, Quevedo I R, Elimelech M, Tufenkji N (2010), Aggregation and deposition of engineered nanomaterials in aquatic environments: Role of physicochemical interactions. Environmental Science and Technology. 44(17): 6532-6549. http://dx.doi.org/10.1021/es100598h.

8   Cullen E, O'Carroll D M, Yanful E K, Sleep B (2010), Simulation of the subsurface mobility of carbon nanoparticles at the field scale. Advances in Water Resources. 33(4): 361-371. http://dx.doi.org/https://doi.org/10.1016/j.advwatres.2009.12.001.

9   Boncagni N T, Otaegui J M, Warner E, Curran T, Ren J, Fidalgo de Cortalezzi M M (2009), Exchange of TiO$_2$ nanoparticles between streams and streambeds. Environmental Science and Technology. 43(20): 7699-7705. http://dx.doi.org/10.1021/es900424n.

10   Indris S, Amade R, Heitjans P, Finger M, Haeger A, Hesse D, Grünert W, Börger A, Becker K D (2005), Preparation by high-energy milling, characterization, and catalytic properties of nanocrystalline TiO$_2$. Journal of Physical Chemistry B. 109(49): 23274-23278. http://dx.doi.org/10.1021/jp054586t.

11   Klaine S J, Alvarez P J J, Batley G E, Fernandes T F, Handy R D, Lyon D Y, Mahendra S, McLaughlin M J, Lead J R (2008), Nanomaterials in the environment: Behavior, fate, bioavailability, and effects. Environmental Toxicology and Chemistry. 31(12): 1825-1851. http://dx.doi.org/10.1897/08-

090.1.

12 Cheng C, Packman A I, Zhang D, Gaillard J-F (2010), A multi-scale investigation of interfacial transport, pore fluid flow, and fine particle deposition in a sediment bed. Water Resources Research. 46(11): W11560. http://dx.doi.org/10.1029/2009WR009018.

13 Chen C, Packman A I, Gaillard J-F (2008), Pore-scale analysis of permeability reduction resulting from colloid deposition. Geophysical Research Letters. 35(7): 199-208. http://dx.doi.org/10.1029/2007GL033077.

14 Datry T, Lamouroux N, Thivin G, Descloux S, Baudoin J M (2015), Estimation of sediment hydraulic conductivity in river reaches and its potential use to evaluate streambed clogging. River Research and Applications. 31(7): 880-891. http://dx.doi.org/10.1002/rra.2784.

15 Chen C, Lau B L T, Gaillard J-F, Packman A I (2009), Temporal evolution of pore geometry, fluid flow, and solute transport resulting from colloid deposition. Water Resources Research. 45(6): 136-148. http://dx.doi.org/10.1029/2008WR007252.

16 Gaillard J-F, Chen C, Stonedahl S H, Lau B L T, Keane D T, Packman A I (2007), Imaging of colloidal deposits in granular porous media by X-ray difference micro-tomography. Geophysical Research Letters. 34(18): 265-272. http://dx.doi.org/10.1029/2007GL030514.

17 Ren J, Packman A I (2005), Coupled stream−subsurface exchange of colloidal hematite and dissolved zinc, copper, and phosphate. Environmental Science and Technology. 39(17): 6387-6394. http://dx.doi.org/10.1021/es050168q.

18 Karwan D L, Saiers J E (2012), Hyporheic exchange and streambed filtration of suspended particles. Water Resources Research. 48(1): 273-279. http://dx.doi.org/10.1029/2011WR011173.

19 Harvey J W, Drummond J D, Martin R L, McPhillips L E, Packman A I, Jerolmack D J, Stonedahl S H, Aubeneau A F, Sawyer A H, Larsen L G, Tobias C R (2012), Hydrogeomorphology of the hyporheic zone: Stream solute and fine particle interactions with a dynamic streambed. Journal of Geophysical Research:

Biogeosciences. 117(G4): 2740-2760. http://dx.doi.org/10.1029/2012JG002043.

20 Anderson E J, Phanikumar M S (2011), Surface storage dynamics in large rivers: Comparing three-dimensional particle transport, one-dimensional fractional derivative, and multirate transient storage models. Water Resources Research. 47(9): 3101-3106. http://dx.doi.org/10.1029/2010WR010228.

21 Battin T J, Kammer F V D, Weilhartner A, Ottofuelling S, Hofmann T (2009), Nanostructured TiO_2: Transport behavior and effects on aquatic microbial communities under environmental conditions. Environmental Science and Technology. 43(21): 8098-8104. http://dx.doi.org/10.1021/es9017046.

22 Kanel S R, Goswami R R, Clement T P, Barnett M O, Zhao D (2008), Two dimensional transport characteristics of surface stabilized zero-valent iron nanoparticles in porous media. Environmental Science and Technology. 42(3): 896-900. http://dx.doi.org/10.1021/es071774j.

23 Lecoanet H F, Wiesner M R (2004), Velocity effects on fullerene and oxide nanoparticle deposition in porous media. Environmental Science and Technology. 38(16): 4377-4382. http://dx.doi.org/10.1021/es035354f.

24 Packman A, Brooks N (1995), Colloidal particle exchange between stream and stream bed in a laboratory flume. Marine and Freshwater Research. 46(1): 233-236. http://dx.doi.org/10.1071/MF9950233.

25 Packman A I, Brooks N H, Morgan J J (2000), A physicochemical model for colloid exchange between a stream and a sand streambed with bed forms. Water Resources Research. 36(8): 2351-2361. http://dx.doi.org/10.1029/2000WR900059.

26 Jin G, Tang H, Li L, Barry D A (2011), Hyporheic flow under periodic bed forms influenced by low-density gradients. Geophysical Research Letters. 38(22): L22401. http://dx.doi.org/10.1029/2011GL049694.

27 Lyon-Marion B A, Becker M D, Kmetz A A, Foster E, Johnston K P, Abriola L M, Pennell K D (2017), Simulation of magnetite nanoparticle mobility in a heterogeneous flow cell. Environmental Science: Nano. 4(5): 1512-1524.

http://dx.doi.org/10.1039/C7EN00152E.

28 Jin G, Tang H, Li L, Barry D A (2015), Prolonged river water pollution due to variable-density flow and solute transport in the riverbed. Water Resources Research. 51(4): 1898-1915. http://dx.doi.org/10.1002/2014WR016369.

29 Kuan W K, Jin G, Xin P, Robinson C, Gibbes B, Li L (2012), Tidal influence on seawater intrusion in unconfined coastal aquifers. Water Resources Research. 48(2): 136-149. http://dx.doi.org/10.1029/2011WR010678.

30 Shen C, Zhang C, Jin G, Kong J, Li L (2016), Effects of unstable flow on solute transport in the marsh soil and exchange with coastal water. Geophysical Research Letters. 43(23): 12091–12101. http://dx.doi.org/10.1002/2016GL070576.

31 Shen C, Jin G, Xin P, Kong J, Li L (2015), Effects of salinity variations on pore water flow in salt marshes. Water Resources Research. 51(6): 4301-4319. http://dx.doi.org/10.1002/2015WR016911.

32 Oostrom M, Hayworth J S, Dane J H, Güven O (1992), Behavior of dense aqueous phase leachate plumes in homogeneous porous media. Water Resources Research. 28(8): 2123-2134. http://dx.doi.org/10.1029/92WR00711.

33 Cardenas M B, Wilson J L (2007), Dunes, turbulent eddies, and interfacial exchange with permeable sediments. Water Resources Research. 43(8): 199-212. http://dx.doi.org/10.1029/2006WR005787.

34 Janssen F, Cardenas M B, Sawyer A H, Dammrich T, Krietsch J, de Beer D (2012), A comparative experimental and multiphysics computational fluid dynamics study of coupled surface–subsurface flow in bed forms. Water Resources Research. 48(8): 8514-8530. http://dx.doi.org/10.1029/2012WR011982.

35 Trauth N, Schmidt C, Maier U, Vieweg M, Fleckenstein J H (2013), Coupled 3-D stream flow and hyporheic flow model under varying stream and ambient groundwater flow conditions in a pool-riffle system. Water Resources Research. 49(9): 5834-5850. http://dx.doi.org/10.1002/wrcr.20442.

36　Chen X, Cardenas M B, Chen L (2015), Three-dimensional versus two-dimensional bed form-induced hyporheic exchange. Water Resources Research. 51(4): 2923-2936. http://dx.doi.org/10.1002/2014WR016848.

37　Sawyer A H, Bayani Cardenas M, Buttles J (2011), Hyporheic exchange due to channel-spanning logs. Water Resources Research. 47(8): 427-438. http://dx.doi.org/10.1029/2011WR010484.

38　Gomez-Velez J D, Krause S, Wilson J L (2014), Effect of low-permeability layers on spatial patterns of hyporheic exchange and groundwater upwelling. Water Resources Research. 50(6): 5196-5215. http://dx.doi.org/10.1002/2013WR015054.

39　FLUENT (2005), FLUENT 6.1 user's Guide, Lebanon, New Hampshire, USA. http://dx.doi.org/jullio.pe.kr/fluent6.1/help/html/ug/main_pre.htm, last accessed 2 July 2018.

40　COMSOL (2015), COMSOL Multiphysics Reference Manual version 5.0. Burlington, MA, USA: COMSOL Inc. http://dx.doi.org/cn.comsol.com/documentation, last accessed 2 July 2018.

41　Packman A I, Brooks N H, Morgan J J (2000), Kaolinite exchange between a stream and streambed: Laboratory experiments and validation of a colloid transport model. Water Resources Research. 36(8): 2363-2372. http://dx.doi.org/10.1029/2000WR900058.

42　Ren J, Packman A I (2004), Modeling of simultaneous exchange of colloids and sorbing contaminants between streams and streambeds. Environmental Science and Technology. 38(10): 2901-2911. http://dx.doi.org/10.1021/es034852l.

43　Areepitak T, Ren J (2011), Model simulations of particle qggregation effect on colloid exchange between streams and streambeds. Environmental Science and Technology. 45(13): 5614-5621. http://dx.doi.org/10.1021/es200586v.

44　Bekhit H M, Hassan A E (2005), Two-dimensional modeling of contaminant transport in porous media in the presence of colloids. Advances in Water Resources. 28(12): 1320-1335.

http://dx.doi.org/10.1016/j.advwatres.2005.04.009.

45 Oz I, Shalev E, Yechieli Y, Gavrieli I, Gvirtzman H (2014), Flow dynamics and salt transport in a coastal aquifer driven by a stratified saltwater body: Lab experiment and numerical modeling. Journal of Hydrology. 511: 665-674. http://dx.doi.org/10.1016/j.jhydrol.2014.02.020.

46 Chang S W, Clement T P (2013), Laboratory and numerical investigation of transport processes occurring above and within a saltwater wedge. Journal of Contaminant Hydrology. 147(2): 14-24. http://dx.doi.org/10.1016/j.jconhyd.2013.02.005.

47 Wang Y, Li Y, Fortner J D, Hughes J B, Abriola L M, Pennell K D (2008), Transport and retention of nanoscale C_{60} aggregates in water-saturated porous media. Environmental Science and Technology. 42(10): 3588-3594. http://dx.doi.org/10.1021/es800128m.

48 Brant J, Lecoanet H, Wiesner M R (2005), Aggregation and deposition characteristics of fullerene nanoparticles in aqueous systems. Journal of Nanoparticle Research. 7(4-5): 545-553. http://dx.doi.org/10.1007/s11051-005-4884-8.

49 Barry DA, Sposito G (1990), Three-dimensional statistical moment analysis of the Stanford/Waterloo Borden tracer data. Water Resources Research. 26(8): 1735-1747. http://dx.doi.org/10.1029/WR026i008p01735.

50 Goswami R R, Clement T P, Hayworth J H (2011), Comparison of numerical techniques used for simulating variable-density flow and transport experiments. Journal of Hydrologic Engineering. 17(2): 272-282. http://dx.doi.org/10.1061/(ASCE)HE.1943-5584.0000428.